Engineering Fracture Mechanics 164 (2016) 1–18

Contents lists available at ScienceDirect

Engineering Fracture Mechanics

journal homepage: www.elsevier.com/locate/engfracmech

Experimental determination of *J*-resistance curves of nuclear steam generator tubes

Marcos A. Bergant [a,*], Alejandro A. Yawny [b], Juan E. Perez Ipiña [c]

[a] Gerencia CAREM, Centro Atómico Bariloche (CNEA), Av. Bustillo 9500, San Carlos de Bariloche 8400, Argentina
[b] División Física de Metales, Centro Atómico Bariloche (CNEA)/CONICET, Av. Bustillo 9500, San Carlos de Bariloche 8400, Argentina
[c] Grupo Mecánica de Fractura, Universidad Nacional del Comahue/CONICET, Buenos Aires 1400, Neuquén 8300, Argentina

ARTICLE INFO

Article history:
Received 23 March 2016
Received in revised form 14 July 2016
Accepted 20 July 2016
Available online 08 August 2016

Keywords:
Fracture toughness
J-resistance curve
Non-standard specimens
Steam generator tubes
Incoloy 800

ABSTRACT

The experimental determination of room temperature *J*-resistance curves of thin walled Incoloy 800 nuclear steam generator tubes was studied. Different non-standard specimens' geometries were considered, including circumferential and longitudinal trough-wall cracks. *J*-integral values were estimated using the η-factor method from the experimental load vs. *LLD* and *CMOD* displacement records. Circumferential cracks led to higher *J*-resistance curves than longitudinal cracks indicating a degree of anisotropy in the fracture properties. Low constraint conditions promoted by predominant tensile loadings gave higher *J*-resistance curves than bending configurations. Details associated with the fatigue pre-cracking procedure and crack length monitoring along the tests are presented.

1. Introduction

Steam generators (SGs) are large heat exchangers consisting in a bundle of thousands of tubes arranged inside a pressure vessel. The steam generator tubes (SGTs) separate the primary and secondary circuits of a nuclear power plant, representing up to 60% of the total primary pressure retaining boundary. In case of a failure giving place to a leakage from the primary to the secondary circuits, a potential release of radioactivity may occur. Therefore, the structural integrity of SGTs has a superlative importance from the safety standpoint [1,2].

In order to assess the significance of SGTs defects, different acceptance criteria has been developed. The firsts were based on limit load analyses which considered plastic collapse as the prevailing failure mode due to the inherent high toughness of the austenitic materials used for SGTs fabrication [2]. However, the assumption on plastic collapse dominance has not been properly validated, mainly due to the lack of specific fracture toughness data for SGTs materials. Furthermore, the experience has demonstrated that those initial criteria are over conservative being this especially noticeable in the case of crack like defects [2]. Responding to this limitation, new criteria have been proposed [3–12]. Instead of performing a direct load limit analysis, they now include fracture mechanics concepts which require the proper assessment of the fracture properties of actual SGTs.

* Corresponding author.
E-mail addresses: marcos.bergant@cab.cnea.gov.ar (M.A. Bergant), yawny@cab.cnea.gov.ar (A.A. Yawny), juan.perezipina@fain.uncoma.edu.ar (J.E. Perez Ipiña).

http://dx.doi.org/10.1016/j.engfracmech.2016.07.008
0013-7944/

Nomenclature

a	crack length or half-crack length
b_0	remaining ligament length
B	specimen thickness
C_i	load vs. displacement compliance
CMOD	crack mouth opening displacement
CTOA	crack tip opening angle
CTOD	crack tip opening displacement
C(T)	compact tension specimen
d_f	coefficient of the blunting line
DCPD	direct current potential drop
E	Young's elastic modulus
EDM	electrical discharge machining
J	J-integral
J_{el}	elastic component of the total J-integral
J_{pl}	plastic component of the total J-integral
K_I	mode I linear elastic stress intensity factor
LLD	load line displacement
LVDT	linear variable differential transformer
M(T)	middle tension specimen
NDRM	normalization data reduction method
P	load
SE(B)	single-edge-notched bending specimen
SE(T)	single-edge-notched tensile specimen
SG	steam generator
SGT	steam generator tube
t	tube wall thickness
T	tunneling magnitude
TIG	tungsten inert gas welding
TWC	through-wall crack
UC	unloading compliance
U_{pl}	plastic work
W	specimen width
Δa	crack growth extension
η	calibration factor
η_{CMOD}	η-factor based on *CMOD*
η_{LLD}	η-factor based on *LLD*
ν	Poisson's ratio
σ_{YS}	yield stress
σ_{UTS}	ultimate tensile strength
σ_f	flow stress

In this context, a research effort is being conducted in the last years by the present authors to obtain specific experimental data of fracture toughness of SGTs [13,14]. The ultimate purpose is the development of a more rational approach for structural integrity assessments of SGTs [15,16].

It is important to remark here that the number of studies reporting SGTs fracture properties is scarce. Only three references could be found in the open literature reporting results from fracture tests using specimens obtained from SGTs [10,13,17,18]. The reasons of this rather limited information might reside in the complexities associated with the development of non-standardized techniques due to the small geometric dimensions and high toughness properties of typical SGTs.

In a previous study, Bergant et al. [14] have considered a comprehensive set of non-standardized SGTs specimens and estimated the J-resistance curves through the evaluation of the η-factor [19] using finite element based numerical procedures. Specimens with circumferential and longitudinal through-wall cracks (TWC) were considered as they represent typical in-service detected defects [1]. Also high and low constraint testing configurations were proposed, by means of bending and tensile prevailing loads, respectively. The validity and applicability conditions of the η-factor for each of the considered geometries were evaluated.

In the present work, the experimental counter-part of the previous numerical study is presented. Thus, the different proposed specimen geometries were now fabricated and experimentally tested. In that way, *J*-resistance curves were estimated for SGTs with circumferential and longitudinal cracks, under high and low constraint conditions.

2. Experimental details

2.1. Material and specimens

Fracture specimens were obtained from Incoloy 800 SGTs (Ni: 30.0–35.0; Cr: 19.0–23.0; Fe: 35.5 min, % in weight) with 15.88 mm external diameter and 1.13 mm wall thickness. The material considered in the present study was Incoloy 800 alloy which is widely used as SGT material due to its excellent corrosion resistance in the particular high temperature environment of nuclear SGs.

The different non standardized fracture specimens considered in the previous work of Bergant et al. [14] are now introduced. Fig. 1(a) shows specimens corresponding to straight portions of tubes and containing one (T1) or two opposite (T2) circumferential TWCs. Specimens T1(T) and T1(B) shown in Fig. 1(b) and (d) refer to those with one circumferential TWC loaded in tension and bending, respectively. T2(T) in Fig. 1(c) represents a specimen with two opposite circumferential TWCs under tension. In the tensile configurations, internal bronze metal plugs were used at both ends of the specimens, following the recommendations of ASTM A370-15 [20] for tensile testing of tubular specimens. In these cases, a hydraulic gripping system equipped with appropriate wedges and controlled gripping regulated pressure was used for clamping the specimen ends.

In Fig. 2, the specimens with longitudinal TWCs are introduced. Obtaining these types of specimens required the design of an ad-hoc fabrication procedure which is outlined in Fig. 2(a). The method developed prevents the introduction of plastic deformation in the central circumferential arc thus keeping the original thermomechanical state of the SGTs in the region of interest, i.e., in the zone where the crack propagation will be characterized. Concerning the specific longitudinal TWCs geometries: Fig. 2(b) shows the single-edge-notched bend SE(B) "O"; Fig. 2(c), the compact like C(T) "X"; Fig. 2(d), the C(T) "O"; Fig. 2(e), the middle tension M(T) "O"; Fig. 2(f), the pin-loaded single-edge tension like SE(T) "X" and Fig. 2(g)

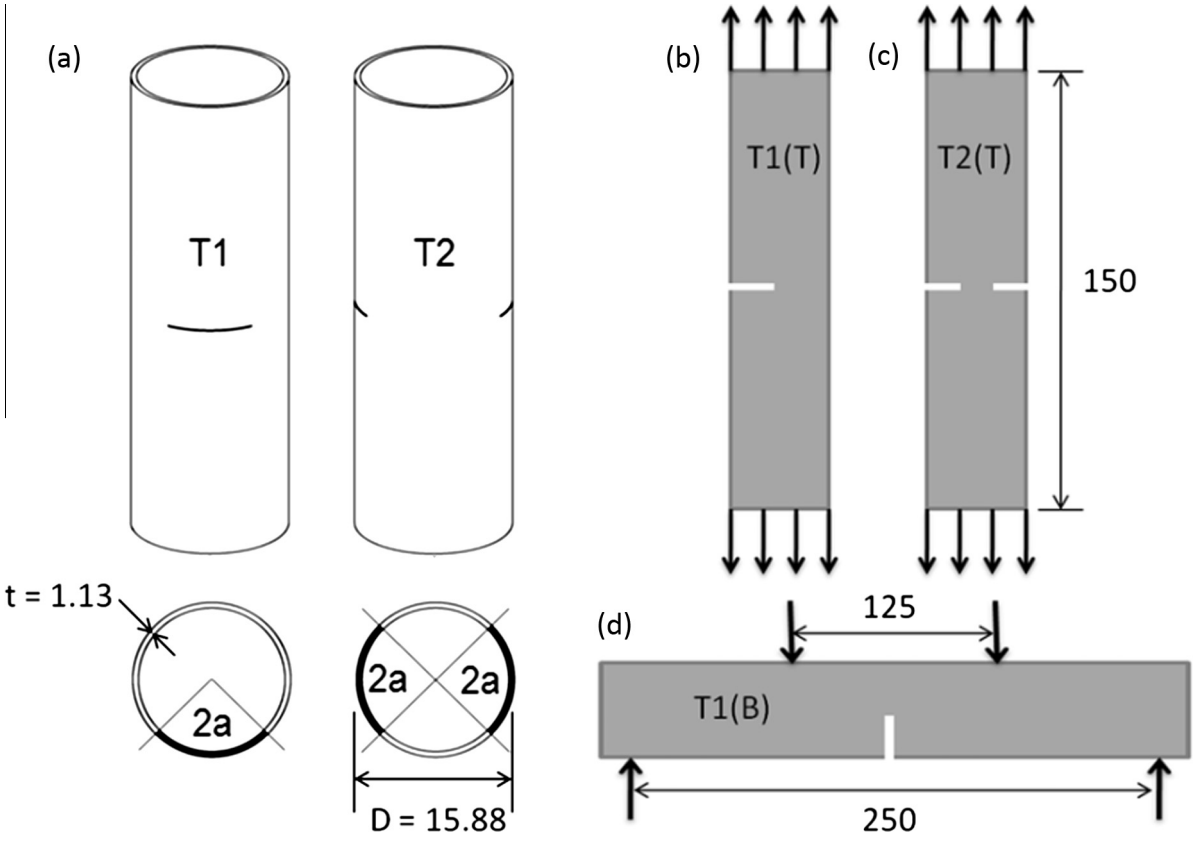

Fig. 1. SGT fracture specimens with one or two opposite circumferential TWCs in tensile (T1(T), T2(T), respectively) and one circumferential TWC in bending T1(B) geometries.

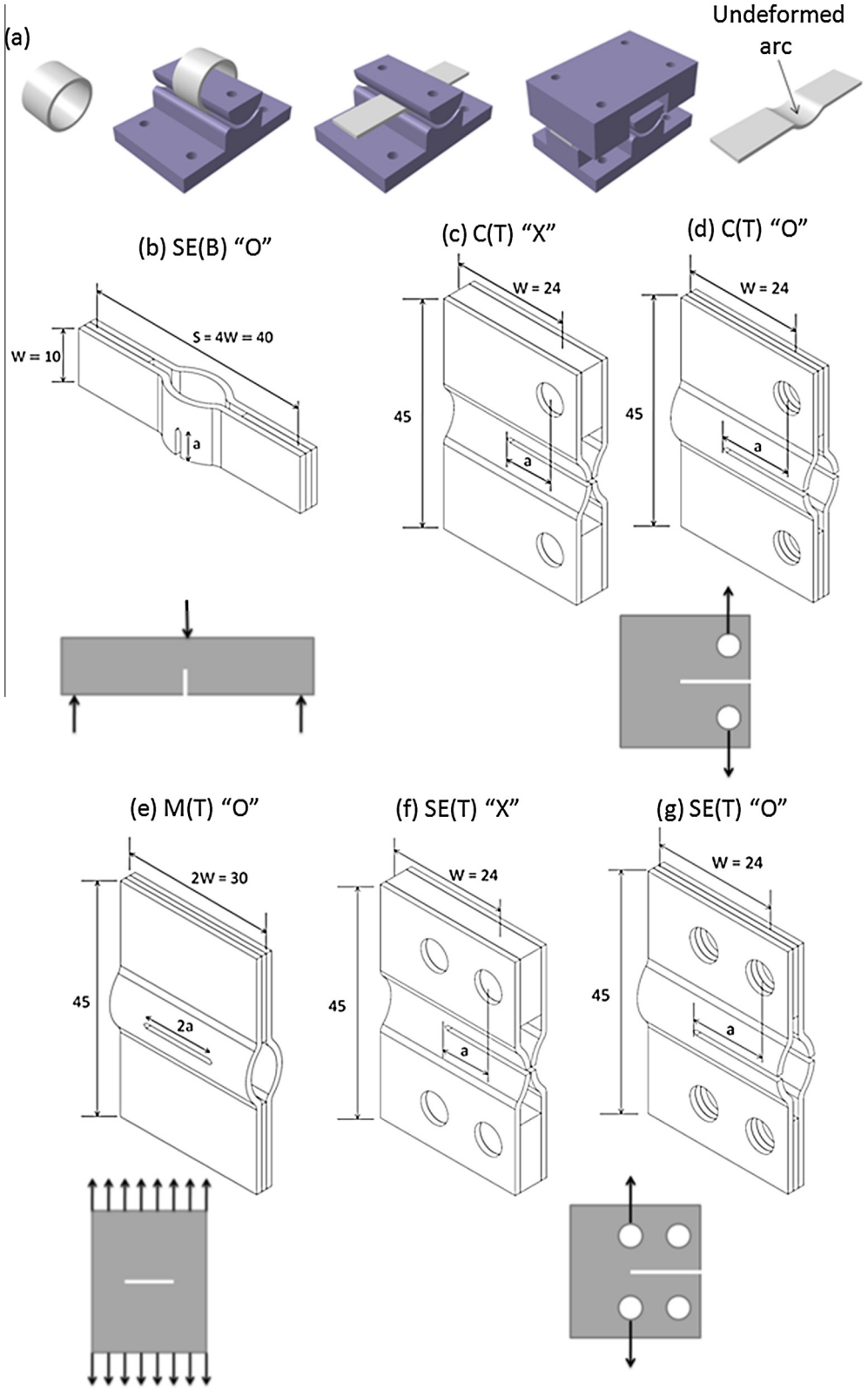

Fig. 2. SGT fracture specimens with longitudinal TWCs in tensile (C(T), SE(T) and M(T)) and bending (SE(B)) geometries.

the SE(T) "O". As can be appreciated from the figures, all longitudinal TWCs specimens consists of two asymmetric hemi-specimens joined on the tube external side ("X" geometries) or internal side ("O" geometries) to constitute a symmetric composite specimen. It can also be seen that in all cases, a third material layer (AISI 304 sheet) was introduced between the two hemi-specimens. This layer was joined to the SGT material using low power TIG welding to provide adequate mechanical stability to the different developed geometries. Special care was taken during the welding procedure to limit the maximum temperature excursion in the region of interest. Images of fabricated longitudinal TWCs SGTs specimens are presented in

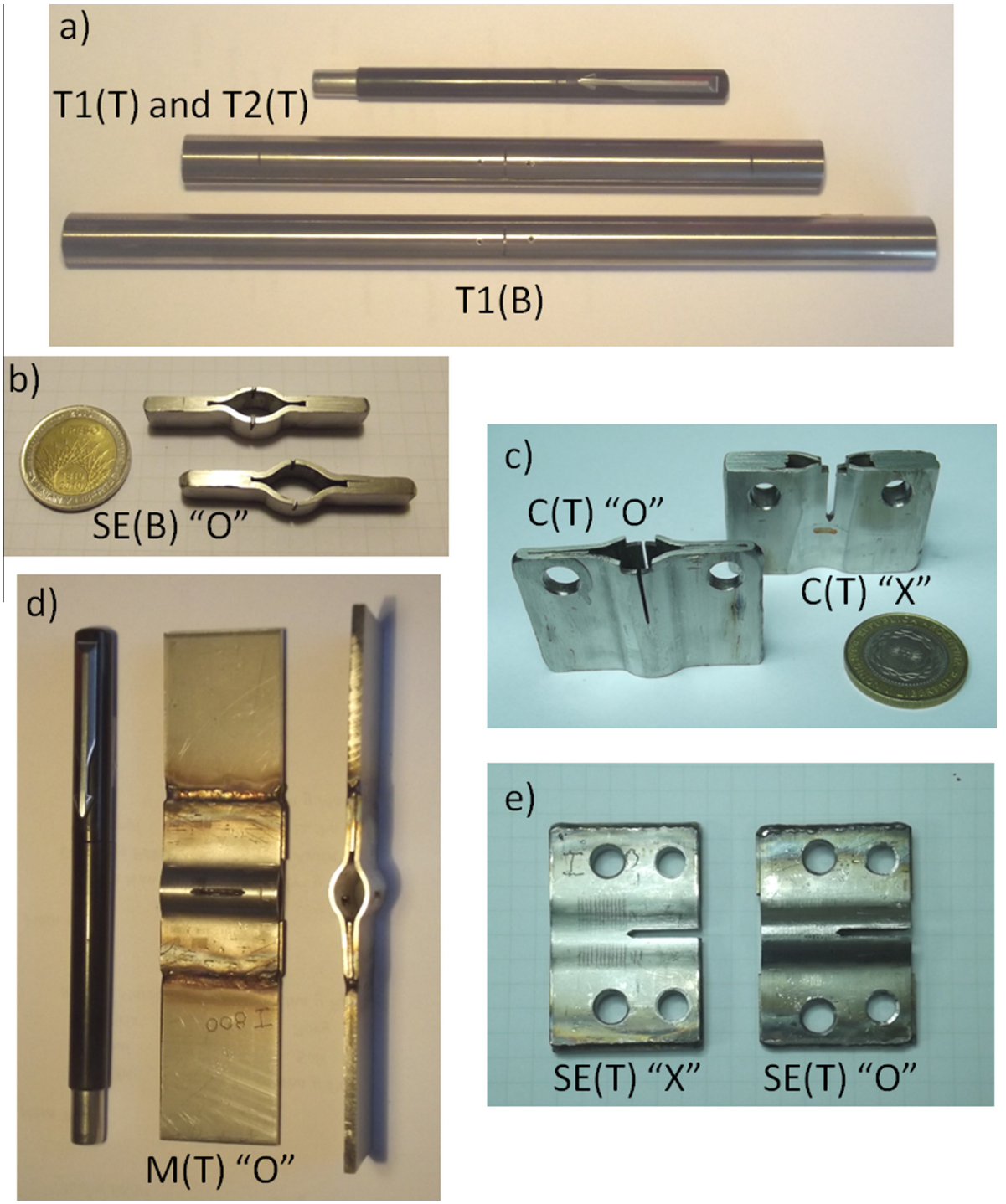

Fig. 3. Images of the fabricated specimens containing circumferential and longitudinal TWCs.

Fig. 3. In the case of the M(T) "O" type of specimen, additional extensions for proper gripping were added as can be seen from the comparison between Figs. 2(e) and 3(d).

2.2. Mechanical testing

In the present work, fracture toughness of SGTs is characterized in terms of *J*-resistance curves. The first reason for that selection is the ductile behavior exhibited by the typical SGTs materials which suggests considering resistance curves based on an elastoplastic fracture mechanics parameter be an adequate option to tackle the problem. On the other hand, the use of the *J*-integral represents an experimental advantage in comparison with other elastoplastic parameters as the *CTOD* or *CTOA*. In effect, while *J* can be directly assessed from experimental load vs. displacement records, the *CTOD* or *CTOA* require additional specific instrumentation such as clip gages or optical devices to measure the progression of the crack opening along the test. Keeping in mind that the final objective is to measure resistance curves at temperature levels representative of plant actual operating conditions, 300 °C approximately, it is clear that the *J*-integral can be easily evaluated in this case, whereas the use of common *CTOD* or *CTOA* instrumentation may result non practical.

All the mechanical tests were performed by loading the specimens under displacement control using servo-hydraulic testing machines MTS 810 and MTS Landmark, both 100 kN maximum load capacity. The applied load *P* and the load-line displacement *LLD* were obtained from the machine LVDT recording piston displacement. The crack mouth opening displacement *CMOD* was measured by means of a clip gage disposed in the way illustrated in Fig. 4 for the different specimen geometries and loading modes considered. In the present work all tests were performed at a room temperature of 24 °C.

Prior to fracture testing, the specimens were firstly notched using electrical discharge machining (EDM) and then fatigue pre-cracked under load control using the above mentioned testing machines. A minimum pre-crack of 1.3 mm was used in

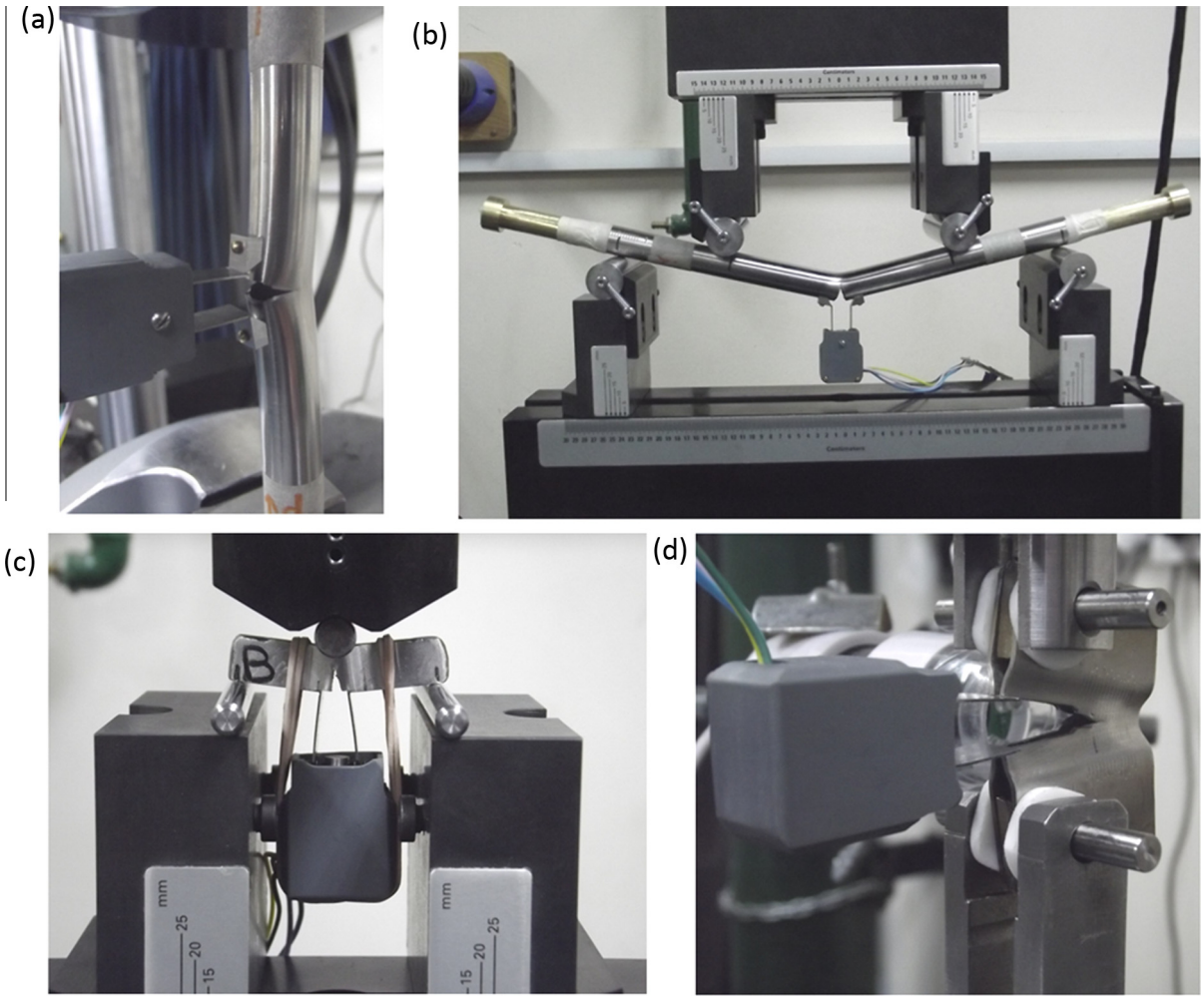

Fig. 4. Experimental arrangement for different fracture specimens: (a) T1(T); (b) T1(B); (c) SE(B) "O"; (d) C(T) "X".

all the cases and the maximum loads during pre-cracking were controlled in order to limit the maximum applied stress intensity factor to $K_I = 40$ MPa $m^{1/2}$. Table 1 summarizes all the fracture tests performed in the context of the present work. For specimens with circumferential TWCs, a and W are half crack length and half mean perimeter of the tube, respectively.

From complementary uniaxial tensile tests performed in original crack free Incoloy 800 tube specimens a yield strength $\sigma_{YS} = 260$ MPa and an ultimate strength $\sigma_{UTS} = 610$ MPa were obtained.

2.3. Construction of J-resistance curves: the η-factor method

The J-integral is usually expressed by separating the elastic and plastic contributions in the form suggested by Rice et al. [19]:

$$J = J_{el} + J_{pl} = \frac{K_I^2}{E/(1-\nu^2)} + J_{pl} \tag{1}$$

Here K_I is the (Mode I) linear elastic stress intensity factor, E is the Young's elastic modulus and ν is the Poisson's ratio. Under certain conditions [19,21], the plastic component J_{pl} can be related to the plastic work area U_{pl} under the P vs. LLD or P vs. $CMOD$ records until the point (P; LLD) or (P; $CMOD$) in the following way:

$$J_{pl} = \eta \frac{U_{pl}}{Bb} \tag{2}$$

where B is the specimen net section thickness, b the uncracked ligament length and η is a calibration factor. U_{pl} is the plastic work calculated from the area under the P vs. LLD or P vs. $CMOD$ records until the point (P; LLD) or (P; $CMOD$). The η-factor is a non-dimensional parameter which is assumed to depend on the geometry and loading type (e.g., bending or tension) but independent of the loading magnitude P. The η-factor is referred to as η_{LLD} or η_{CMOD}, depending whether it is defined in terms of P vs. LLD or P vs. $CMOD$ records, respectively.

Eq. (2) is valid for stationary, i.e., non-growing cracks, in which the non-linearity between the load vs. displacement record is only due to plastic deformation. When there is stable crack growth during the test, a new contribution to non-linearity appears and the J-integral value must be corrected. The correction is performed through a γ-factor that can be derived from η_{LLD} functions [22]. On the other hand, if J-integral values are calculated using the η_{CMOD} definition, the γ-factor is not always valid and the correction cannot be performed [14]. Besides that, it should be pointed out here that such corrections, in case of being considered, would result in J_{pl} values differing less than 15% for the maximum crack growths. Therefore, in order to facilitate the comparison between J-integral values obtained from η_{LLD} and η_{CMOD} definitions, the crack growth corrections were not applied in this work.

In a previous study, J-resistance curves were estimated for T1(T) and T2(T) Incoloy 800 SGTs specimens [13]. In the particular case of the T1(T) specimens, relatively shallow cracks were used ($a/W \sim 0.25$). This led to widespread plasticity and geometric distortion in the specimens. In that study also a numerical estimation of the η-factor was performed, showing that for shallow cracks the η-factor method is not applicable. This conclusion motivated a further study focusing now on deep cracks and high constraint testing configurations in order to ensure the validity of the η-factors performed in [14]. The values of the η_{LLD} and η_{CMOD} taken from [14] for the different specimens geometries and loading modes introduced in Figs. 1 and 2, except for SE(T) specimens, are reproduced for convenience in the present work in Fig. 5 for a/W ratios between 0.4 and 0.7. The η-factors for SE(T) were estimated using the same procedure reported in [14] and were added to Fig. 5.

Table 1
Fracture tests performed in Incoloy 800 SGTs at room temperature (24 °C).

Specimen	a/W	W (mm)
T1(T)	0.26	23.16
T1(T)	0.23	23.16
T1(T)	0.25	23.16
T1(T)	0.27	23.16
T1(T)	0.52	23.16
T1(T)	0.51	23.16
T2(T)	0.53	23.16
T2(T)	0.48	23.16
T2(T)	0.48	23.16
T1(B)	0.44	23.16
T1(B)	0.51	23.16
C(T) "O"	0.54	24.20
C(T) "X"	0.43	23.93
C(T) "X"	0.45	24.03
SE(B) "O"	0.53	9.15
SE(B) "O"	0.51	9.68
SE(T) "X"	0.44	23.86

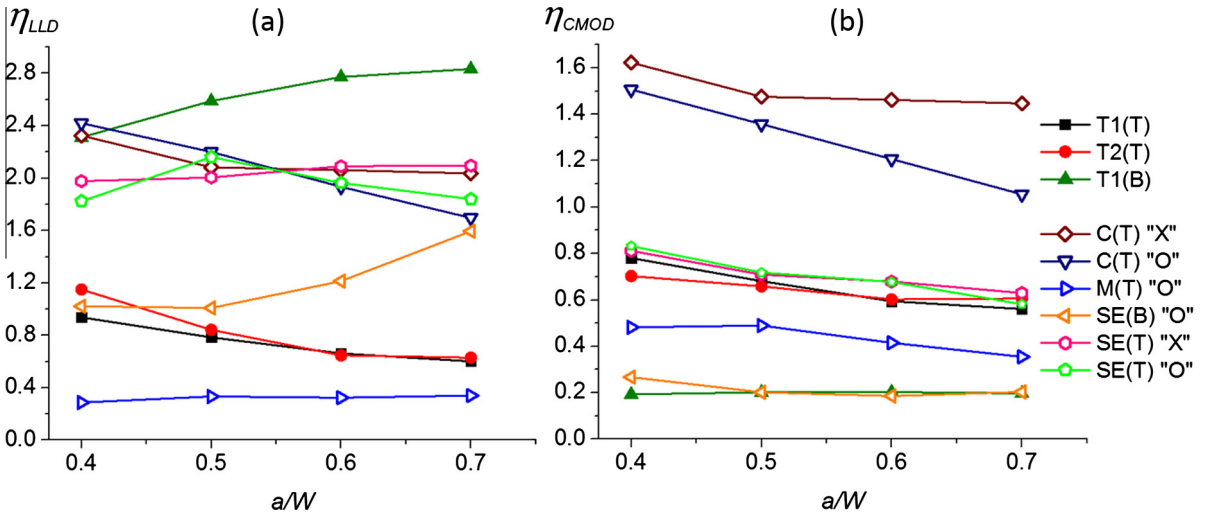

Fig. 5. (a) η_{LLD} and (b) η_{CMOD} factors for the different fracture specimens geometries and loading modes introduced in Figs. 1 and 2 taken from [14].

It should be mentioned that η_{CMOD}-factors were numerically calculated considering the CMOD defined in the theoretical crack mouth [14]. As this CMOD is impractical to measure, the CMOD were determined using clip gages mounted in positions that do not correspond with the numerical definition. Therefore, CMOD corrections were needed to correlate the experimental measurements with the theoretical definition used in [14].

3. Results

3.1. Crack development during the pre-cracking stage

Fig. 6 shows photographs of fracture surfaces of some of the specimens tested in the present work. A variety of cracks front profiles shapes associated with the different geometries and loading conditions can be appreciated from the images. As a general trend, specimens with circumferential TWCs exhibited straight fronts normal to the tangential direction after pre-cracking, Fig. 6(a), while specimens with longitudinal TWCs developed crack fronts inclined to the surface, Fig. 6(b) to (d). The later effect can be understood in terms of the elastic stress fields generated in the crack front at the inner and outer surfaces points, for example for C(T) and M(T) specimens in Fig. 6(c) and (d). Omitting the stress concentration effect at the crack front, the applied force P produces a stress condition that can be interpreted as the superposition of a tensile component, a bending contribution in the specimen's plane and a bending component in a plane normal to the specimen which is introduced by the misalignment between the loading line and the resisting section due to the curvature of the original tube. Thus, while the tensile and in plane bending components lead to uniform stresses at the crack front, the bending component normal to the specimen produces a stress gradient that ranges from tension in the inner side of the tube to compression in the outer side. It is then expected that during fatigue cycling, the crack front growth velocity be non-uniform with the front in the inner surface of the tube growing more rapidly than in the outer side which results in a pre-crack inclined relative to the specimen's surfaces. The effect of the out of plane bending component is much stronger in the M(T) specimen than in the C(T) specimens. This resulted in an uneven growth of the pre-crack from the initial notch as can be seen in Fig. 6 (d). In order to reduce this effect, different positive and negative values of stress ratios R were employed along the pre-cracking procedure. However, the results obtained were not satisfactory and this led to disregard using M(T) specimen for fracture testing. For the same reason, SE(T) type of specimens were pre-cracked as a C(T) specimen and were further tested in the SE(T) configuration.

3.2. Crack length determination during the fracture test

3.2.1. Direct optical method

The construction of the J-resistance curves requires the estimation of the J-integral value and the measurement of the stable crack extension Δa throughout the entire tests. The first method used in the present work was an optical technique. Here it is assumed that a representative value of the extension of the crack front can be obtained by measuring the crack length at the surface of the specimen [13]. A digital microscope was used to detect the crack tip, Fig. 7(a). To facilitate the length measurement, a set of parallel lines with a separation of 0.32 mm were marked on the surface in the direction normal to the expected crack propagation plane. In Fig. 8 images corresponding to the progression of a test in a T1(T) specimen are presented. They illustrate the typical stages observed during the stable crack growth process in ductile materials.

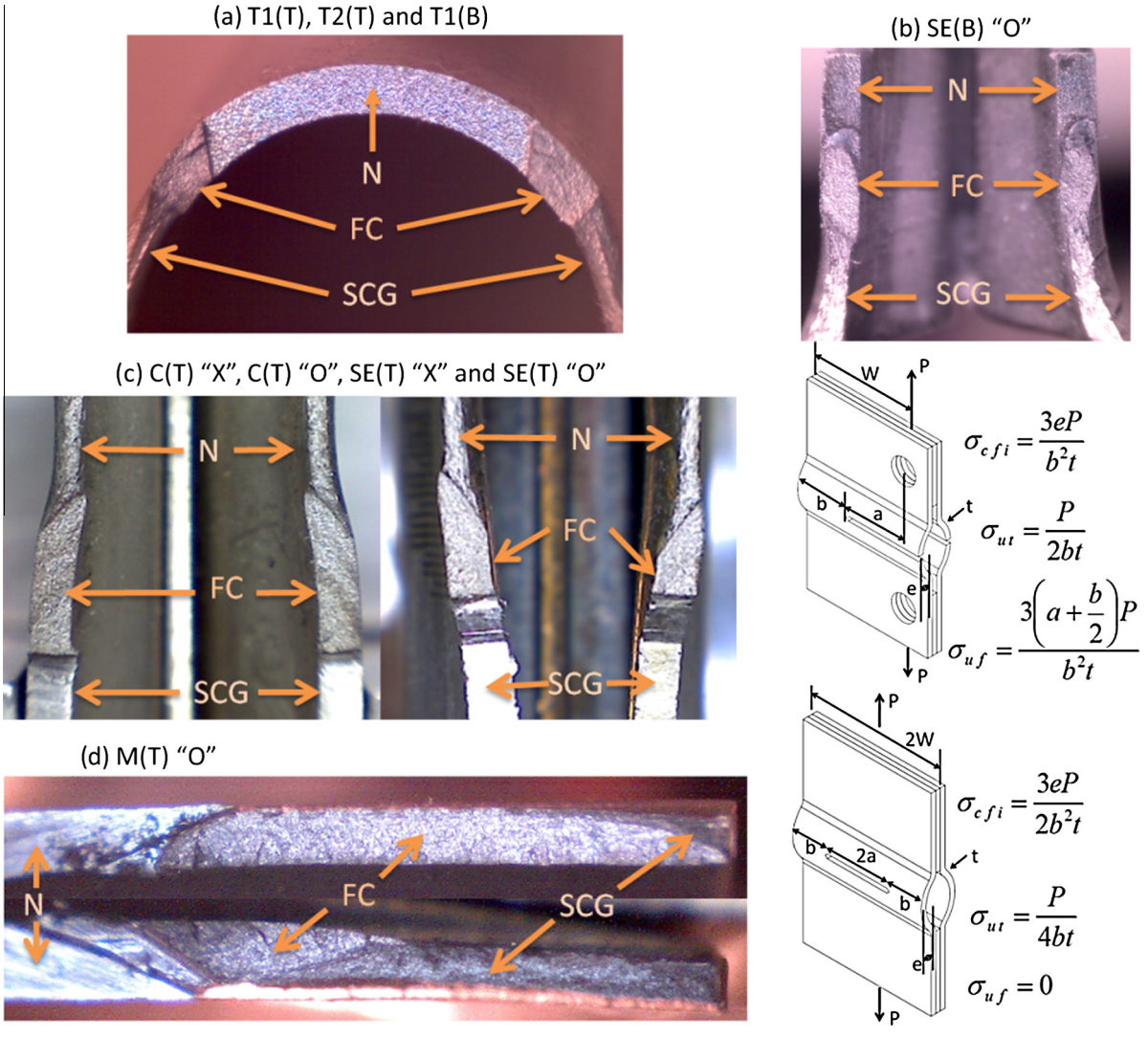

Fig. 6. Fatigue pre-cracking for different specimens (N: electric discharge machining induced notch, FC: fatigue crack, SCG: stable crack growth).

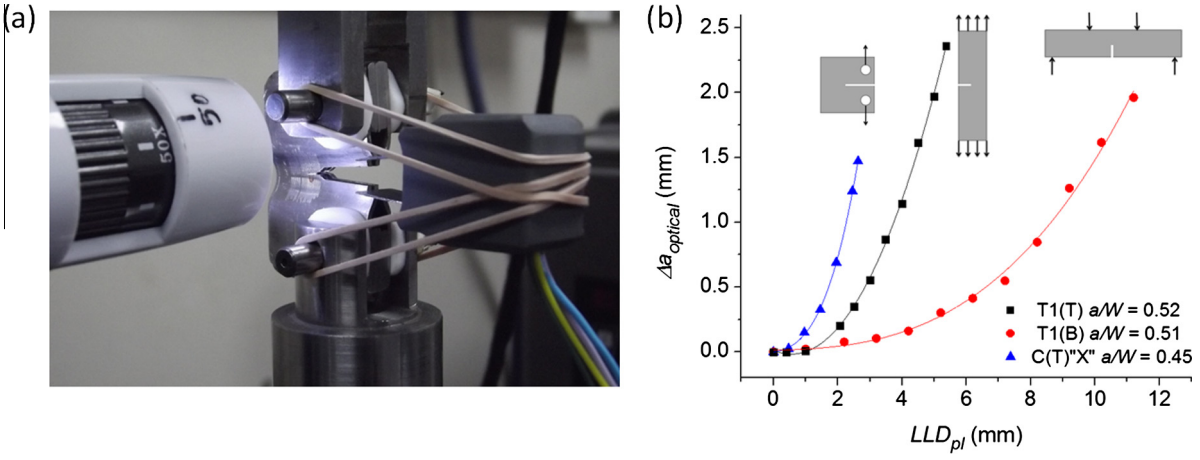

Fig. 7. (a) Digital microscope used for the optical technique during a C(T) "X" test; (b) typical results of $\Delta a_{optical}$ vs. LLD_{pl}.

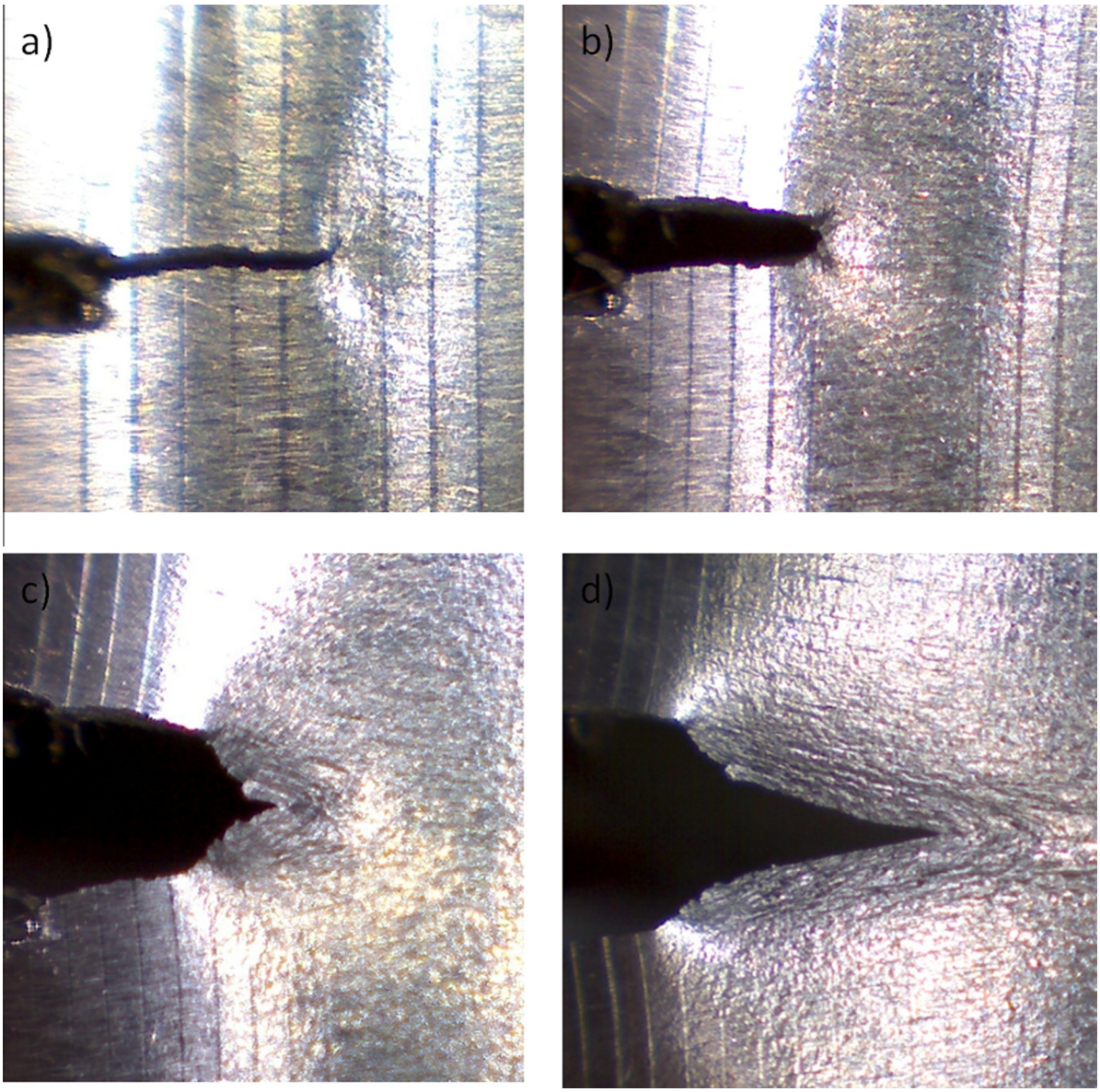

Fig. 8. Images obtained during a T1(T) test used to evaluate the crack length extension: (a) crack opening; (b) crack tip blunting; (c) initiation of stable growth; (d) stable growth.

The crack front extension was determined by analyzing consecutive digital images acquired at increasing imposed displacements. The crack growth was determined measuring the distance between two parallel lines extrapolated from the undeformed region, one located in the crack front and other in the original crack tip position. All the individual crack tips (four in the case of T2(T) specimens and two for the other specimens) were monitored during a specific test and an average value was used to determine the representative crack length a of the specimen. Typical results are shown in Fig. 7(b) for three of the considered geometries. In general, the crack fronts exhibited an even growth for all specimens with maximum differences in crack lengths below 20%, approximately.

As mentioned before, the C(T) and SE(T) type specimens developed inclined pre-crack fronts due to uneven growth. In the case of the "X" configurations, crack growth is faster in the external surface of the specimens which corresponds to the inner side of the initial SG tube. Once the crack is opened, the front in the inner surface of the specimen can be also visualized with the microscope, as shown in Fig. 9(a). The arrows indicate the position of the crack front in each surface. In this way, the relative extension of both fronts can be determined and an average value could be defined in these cases. Fig. 9(c) presents the evolution of the tip extension on both the internal and external surfaces of the specimen. Initially, the tip on the internal

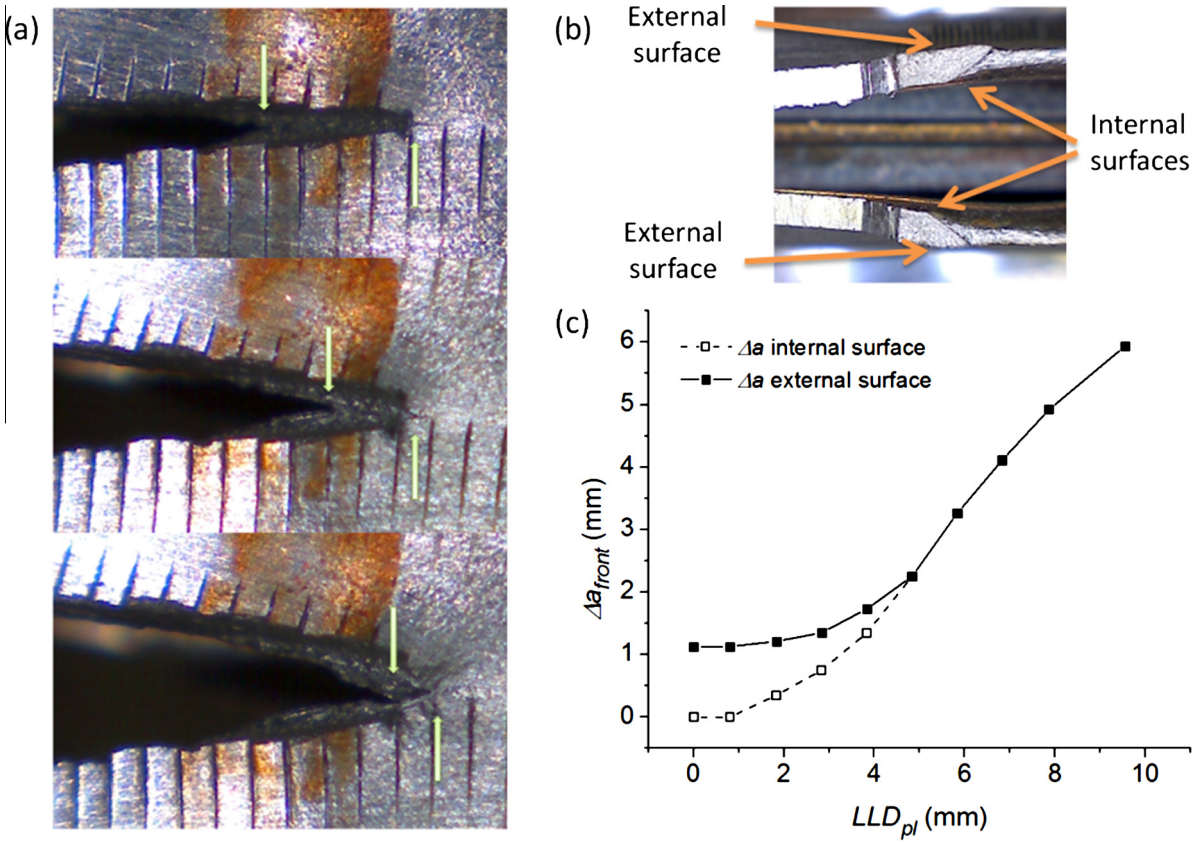

Fig. 9. (a) and (b) Crack tip location in outer and inner surfaces of the tube; (c) results of Δa_{front} vs. LLD_{pl} in a C(T) "X" specimen with $a/W = 0.43$.

side grows more rapidly than the outer tip but, after a certain amount of growth (approximately $\Delta a = 2.2$ mm in Fig. 9(c)) they level out.

For the "O" configurations instead, the front at the inner surfaces could not be observed during the tests as it remains hidden by the external surface during crack opening. However, a similar behavior to the "X" configuration was assumed and the average crack length was also estimated using corrections based on results like those presented in Fig. 9(c). As it will be explained next, this procedure led to very similar *J*-resistance curves for C(T) "O" and C(T) "X" specimens.

3.2.2. Tunneling effects

Observation of the fracture surface corresponding to the first tests indicated the occurrence of crack front tunneling. This cast some doubts about the appropriateness of obtaining representative crack lengths using the optical method described in the previous section. Therefore, in order to assess on the significance of crack tunneling effects on the non-standardized testing techniques here developed, experiments consisting in several stages of crack extension interspersed with crack-front marking stages were conducted. The crack extension stages were performed under displacement control while fatigue crack growth (load ratio $R \sim 0.8$, maximum load 80% of fracture load, 1000–3000 cycles) was employed for crack-front marking. These conditions result in a minimum crack extension which is however enough to demark the actual crack front profile. Fig. 10 presents the results corresponding to this type of tests performed on a T1(T) specimen. In this case, five crack extensions steps (regions 1–5) can be identified between the fatigue pre-crack zone at the left and the surface corresponding to the final fracture at the right in Fig. 10(a). In passing, another feature that can be observed from Fig. 10(a) is the thinning of the tube wall thickness which decreased from its original value of 1.13 mm to 0.3 mm, approximately, after fracture. The severity of the tunneling effect was characterized by defining the parameter $T = a_2 - (a_1 + a_3)/2$ according to the inset in Fig. 10(b). The parameter T is plotted against the total crack extension Δa_1 on the outer surface of the tube in Fig. 10(b) (both variables were normalized with the initial tube wall thickness t). Analysis of the figure indicates that the crack front tunneling develops rapidly at the beginning of the stable crack growth reaching a constant value for crack extensions $\Delta a_1 \sim t$. These results are in line with previous studies of Dawicke and Sutton [23] and James and Newman [24].

In order to establish whether the error magnitude in the optical measurements due to the tunneling effect is acceptable or not, the criterion defined in ASTM E1820-15 [25] for crack length extension prediction was adopted here. Therefore, if the difference between the crack extension measured in the outer surface by means of the optical method Δa_1 and the mean

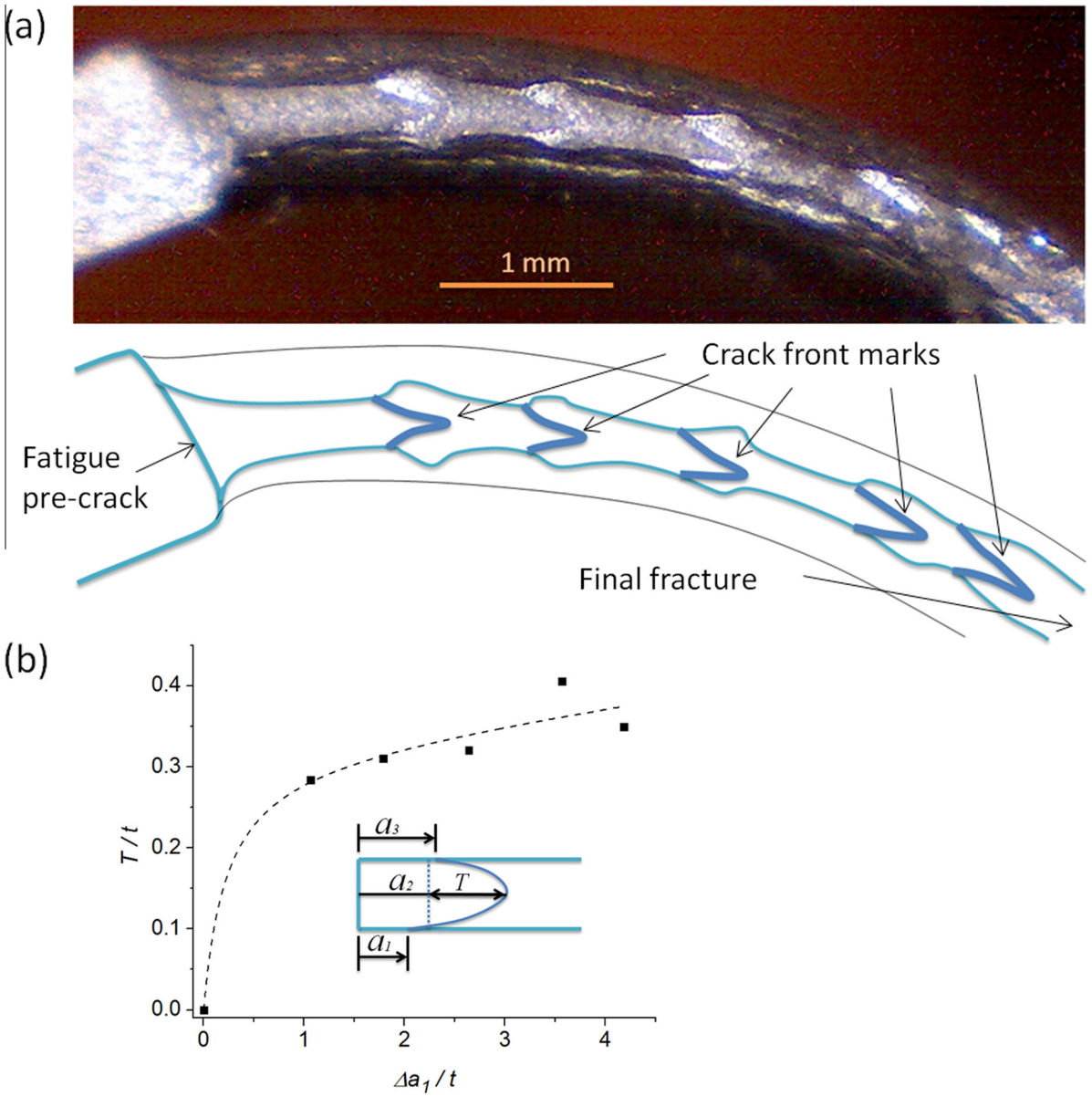

Fig. 10. Evidence of crack tunneling effects during fracture test in a T1(T) specimen with $a/W = 0.52$: (a) crack fronts profiles during stable growth denoted by high R fatigue cycling; (b) evolution of crack front tunneling severity with the test progress (see text for details).

crack extension Δa is lower than 0.15 Δa, the value Δa_1 is considered acceptable and the optical method is suitable. Assuming that $T/2$ is an approximation to the difference between Δa and Δa_1, the previous condition can be restated as $T/2 < 0.15\ \Delta a$. Considering that the ratio T/t reaches values close to 0.3 (Fig. 10(b)), it can be concluded that for a wall thickness $t = 1.13$ mm, the error attributed to the optical method due to the tunneling effect is acceptable from extensions higher than 1 mm, approximately. These results confirm that, in the context of the present work and for near room temperature testing conditions, the direct optical method provides an adequate value of the crack length extension. It is important to mention here that the tunneling severity observed in the other specimens was always lower than that corresponding to the T1(T) case just analyzed, Fig. 10(a). Despite this, the crack front straightness criterion in ASTM E1820-15 [25] is not verified by the tunneled crack fronts.

3.2.3. Normalization data reduction method

Even when the optical technique gave acceptable results for room temperature tests, it presents the disadvantage of being difficult to implement in high temperature tests due to limitations to the maximum working temperature of the involved

devices. Although the later condition is not addressed in this work, obtaining fracture properties of SGTs at 300 °C, i.e., at temperatures corresponding to actual conditions, is the aim of incoming research. Due to that, the convenience of using the Normalization Data Reduction Method (NDRM) [25] was analyzed in the present work. This NDRM has the inherent advantage of allowing obtaining *J*-resistance curves from a single *P* vs. *LLD* experimental record thus avoiding the use of additional crack length measuring equipment. The possibility of implementing such a method constitutes a significant advantage in situations like aggressive environments or high loading rate testing conditions where the use of other techniques is impractical or not feasible. The method is based on a material key curve represented by a deformation dependent function with an explicit functional form. If an appropriate functional form is assumed, the instantaneous crack length value can be determined from corresponding load and displacement values [26].

The NDRM procedure used in this work is based in the Annex 15 of ASTM E1820-15 [25] standard and is described in what follows. The loads *P* and displacements *LLD* up to maximum load are normalized using equations based on the blunted corrected crack length a_{bi}:

$$P_{Ni} = \frac{P_i}{W B \left(\frac{W-a_{bi}}{W}\right)^{\eta_{pl}}} \tag{3}$$

$$LLD'_{pl\,i} = \frac{LLD_{pl\,i}}{W} = \frac{LLD_i - P_i\,C_i}{W} \tag{4}$$

$$a_{bi} = a_0 + \frac{J_i}{d_f\,\sigma_f} \tag{5}$$

where C_i is the elastic compliance for blunted crack length a_{bi}, a_0 is the initial crack length, d_f is the coefficient of the blunting line given by $J = d_f\,\sigma_f\,\Delta a$ and σ_f is the flow stress defined as the average of the yield strength σ_{YS} and the ultimate tensile strength σ_{UTS}. The J_i value is calculated from Eq. (1). The coordinates of the final data point are also normalized with Eqs. (3)–(5) but using the final crack length a_f measured on the fracture surface.

The normalized data set is plotted as shown in Fig. 11 (open symbols). A line tangent to curve is then drawn from the final data point (dotted line). The points located between the point of tangency and the final data point are excluded for the fitting procedure. Data with normalized displacement LLD'_{pl} lower than 0.001 are also excluded. The remaining data are then fitted to a rational function of the form:

$$P_N = \frac{A + B\,LLD_{pl\,i} + C\,LLD^2_{pl\,i} + D\,LLD^3_{pl\,i} + E\,LLD^4_{pl\,i}}{F + LLD_{pl\,i}} \tag{6}$$

Here *A*, *B*, *C*, *D*, *E* and *F* are fitting coefficients. It should be remarked that the fitting function provided in ASTM E1820-15 [25] considers $D = E = 0$. The use of a polynomial of higher order was adopted in this work in order to obtain fittings with maximum deviations below 1% for the final data point (solid line). As can be seen, there is a very good agreement between the normalized data and the fitting function.

By means of an iterative procedure, the crack lengths a_i are inferred for each *P* vs. *LLD* pair equating the expressions for P_N, i.e., Eqs. (3) and (6). Therefore, the *J*-resistance curve can be drawn from the individual *J*-integral values calculated with Eq. (1).

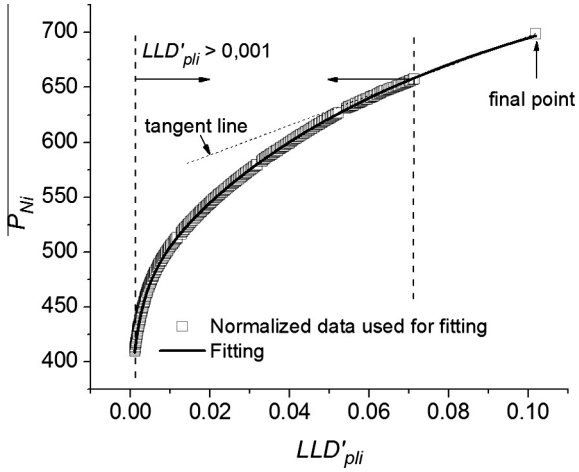

Fig. 11. Use of the NDRM for crack length determination: fitting of normalized data corresponding to a tests in a T1(T) specimen with $a/W = 0.52$.

In order to evaluate the suitability of the NDRM, the stable crack growth extensions predicted by the normalization method were contrasted in Fig. 12 with those determined with direct optical measurements for several fracture tests performed at room temperature. It can be seen that most of the data points fall within a scatter band of ±0.2 mm around the ideal 45° line. Furthermore, as this method uses the initial and final crack lengths measured directly on the fracture surface, these values are precisely estimated from the iterative procedure.

Despite these results seem acceptable, one shortcoming related with the NDRM is that the crack length estimations close to initiation can be extremely sensitive to the normalization function and the data points used to fit it, as well to the blunting expression adopted [26]. In fact, errors in ±0.2 mm for crack extensions will strongly affect the definition of the initiation of stable crack growth, as will be seen later. Fortunately, for engineering problems where ductile crack growth initiation does not normally constitute a critical failure event, the definition of initiation values is not relevant [26]. In these cases, a more consistent alternative is to characterize the fracture toughness by means of *J*-resistance curves or using single parameters describing the toughness after some amount of stable crack growth, e.g., the $J_{1\mathrm{mm}}$ parameter that is defined as the toughness value after 1 mm of stable crack growth [26]. In this context, the NDRM technique can be considered acceptable for the estimation of *J*-resistance curves at high temperature and for crack growths around 1 mm onward.

Unloading compliance (UC) and direct current potential drop (DCPD) techniques were also explored in the present work as candidate techniques to estimate the crack length in some tests. In the case of UC, the compliance showed a decrease at the beginning of the test which was followed by an increase with the crack length growth. This particular behavior was attributed to a friction effect in the loading fixture that causes the apparent negative crack growth in the first stages of the loading [26].

On the other hand, the DCPD technique led to overestimations of crack lengths in comparison with the direct optical method. The calibration function used to correlate the crack length and the electric potential drop along the cracked section was developed in specimens with fatigue grown cracks, i.e., with limited associated plastic deformation. As was shown in Fig. 10, the stable crack growth during fracture tests is accompanied by severe plastic deformation and tube wall thinning. Therefore, it is believed here that the overestimation is due to the increase of the electrical resistivity of the material due to cold work, in agreement with Wilkowski and Maxey [27], and due to the reduction of the cross section associated to wall thinning. As DCPD depends on the effective cross section area [28], wall thinning will introduce extra contributions besides those corresponding to actual crack length increments.

4. Discussion

4.1. J-R curves

Fig. 13(a) and (b) presents *J*-resistance curves obtained for the tested specimens with circumferential and longitudinal TWCs. Only representative curves were included because *J*-resistance curves for similar specimen type and similar a/W ratio were found to be highly reproducible. Symbols correspond to experimental data points obtained with the direct optical method, while lines correspond to power fittings of them. In order to compare the curves for different specimens, the *J*-resistance curves were plotted vs. the individual crack tip extension, Δa. A blunting line was included in the plots with $d_f = 5$, calculated from the yield strength and ultimate tensile strength values using the proposal of Landes [29]. Such high value of d_f, compared with the typical value of 2 reported in ASTM E1820-15 [25], can be attributed to the remarkable strain hardening characteristics exhibited by the material considered here [26].

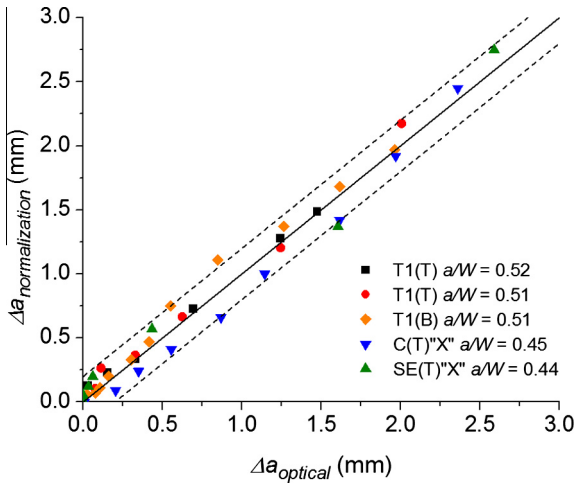

Fig. 12. Comparison between crack extensions estimated by the NDRM and the corresponding values obtained by direct optical measurements.

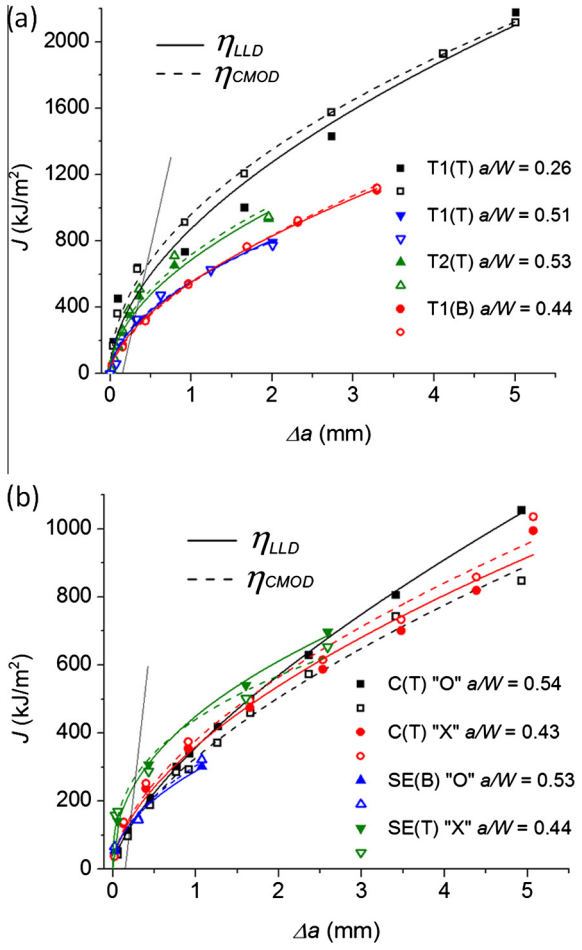

Fig. 13. *J*-resistance curves for (a) circumferential and (b) longitudinal TWCs.

Fig. 13(a) and (b) also compare the *J*-resistance curves obtained through η_{LLD} or η_{CMOD} definitions discussed previously [14], plotted with closed and open symbols, respectively. In particular, Fig. 13(a) shows results for T1(T), T1(B) and T2(T) tests with $a/W \sim 0.5$ together a curve for a T1(T) specimen with $a/W = 0.26$. It can be seen that the tests with deeper cracks results in *J*-integral values almost identical for both η-factors while the curves for the shallow cracked specimen ($a/W = 0.26$) show some difference at the beginning of stable crack growth that diminishes with Δa. This trend may be due to the dependence of the η-factors with the load level, especially for relative shallow cracks, low constraint conditions and η_{LLD} definition [14]. In this case, the use of an average value for η_{LLD} may result imprecise, being the cause of the difference between the η_{LLD} or η_{CMOD} curves at low extensions and shallow cracks.

The results in Fig. 13(a) evidence the effect of the level of constraint on the *J*-resistance curves. As a general trend, tensile loadings with lower levels of constraint give higher curves than bending configurations with higher constraint conditions.

Fig. 13(b) presents the *J*-resistance curves for C(T) "X", C(T) "O", SE(B) "O" and SE(T) "X" specimens with longitudinal TWCs and $a/W \sim 0.5$. Again, the *J*-integral values obtained with η_{LLD} and η_{CMOD} result similar. It can also be seen that the curves for C(T) "X" and C(T) "O" specimens are comparable. This allows concluding that the "X" and "O" configurations lead to equivalent results.

The previous results confirm that the η_{LLD} and η_{CMOD} definitions lead, from a practical standpoint, to the same *J*-integral values for the here proposed specimens provided the cracks are deep, i.e., $a/W \sim 0.5$.

On the other hand, the comparison of Fig. 13(a) and (b) shows that the *J*-resistance curves are higher for circumferential than for longitudinal TWCs. This demonstrates the existence of anisotropy effects in the crack growth resistance of the SGTs under study.

It should be noted that the η-factors used to plot the curves in Fig. 13 were obtained using numerical results up to maximum values for *J*-integral between 500 and 1200 kJ/m^2, as discussed in [14]. Therefore, the curves are strictly valid in this range of *J*-integral values, and should be limited accordingly, i.e., approximately up to 1200 kJ/m^2 for T1(T), 800 kJ/m^2 for T2(T), 600 kJ/m^2 for T1(B), 900 kJ/m^2 for C(T) and SE(T), and 500 kJ/m^2 for SE(B) [14].

For the same reason, the η-factors in Fig. 5 and J-resistance curves presented in Fig. 13 are strictly valid for the tube and specimen geometries used in [14] and in this work.

4.2. Deformation and geometrical distortion of specimens

Fig. 14 presents images of specimens with circumferential TWCs after the fracture tests. The development of geometric distortions can be appreciated. Fig. 14(a) compares the deformation in T1(B) and T1(T) specimens with $a/W \sim 0.5$. It can be noticed that the plastic deformation is contained in the region near the cracked section in the case of the T1(B) specimen. On the contrary, in the case of the T1(T) specimen, the plastic zone spread over a length of between two to three diameters on either side of the cracked section, Fig. 14(b). Similarly, Fig. 14(c) shows that the plastic deformed region in T2(T) specimens extended over a length of one diameter, approximately. In the tensile configurations, T1(T) and T2(T), the plastic deformation occurs in a manner in which the remaining ligament tends to align to the loading axis. This effect explains the development of a bending load component which is normal to the crack plane. Fig. 14(d) presents macrographs of the respective cracked sections, where the initial notch, the fatigue pre-crack and the stable crack growth zones are indicated. It can be observed that the T1(B) specimen maintained the circularity while T1(T) and T2(T) specimens exhibited a more elliptical perimeter.

Fig. 15 depicts some examples of macroscopic plastic deformation development in specimens with longitudinal TWCs. Fig. 15(a) presents a SE(T) "O" specimen after a fracture tests until a stable crack growth $\Delta a \sim 3$ mm. A noticeably opening of the crack accompanied by a change in the radius of initial curvature of the tube can be appreciated. Fig. 15(b) compares

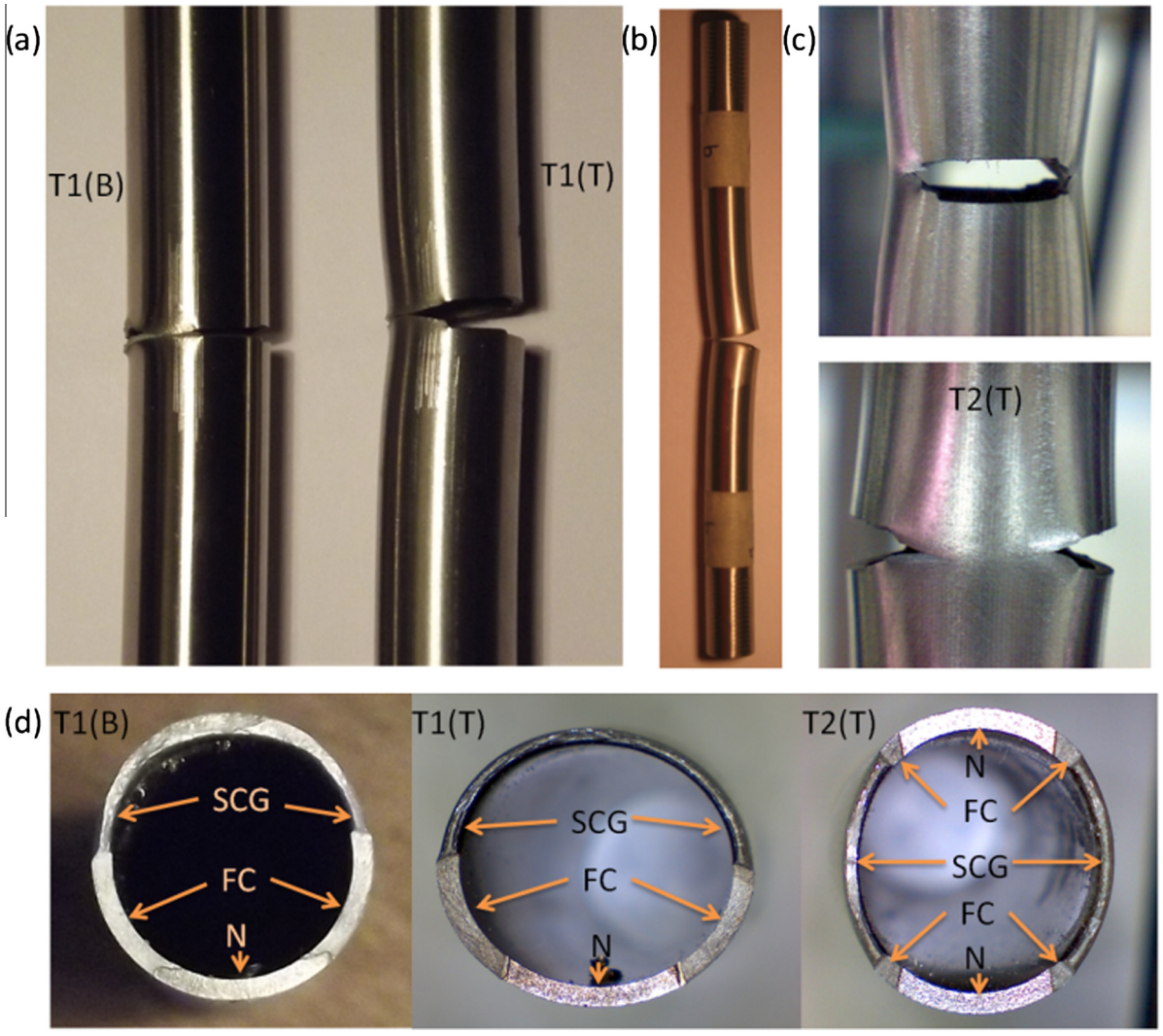

Fig. 14. Macroscopic extension of plastic deformation and associated geometrical distortion in specimens with circumferential TWCs (N: electric discharge machining induced notch, FC: fatigue crack, SCG: stable crack growth).

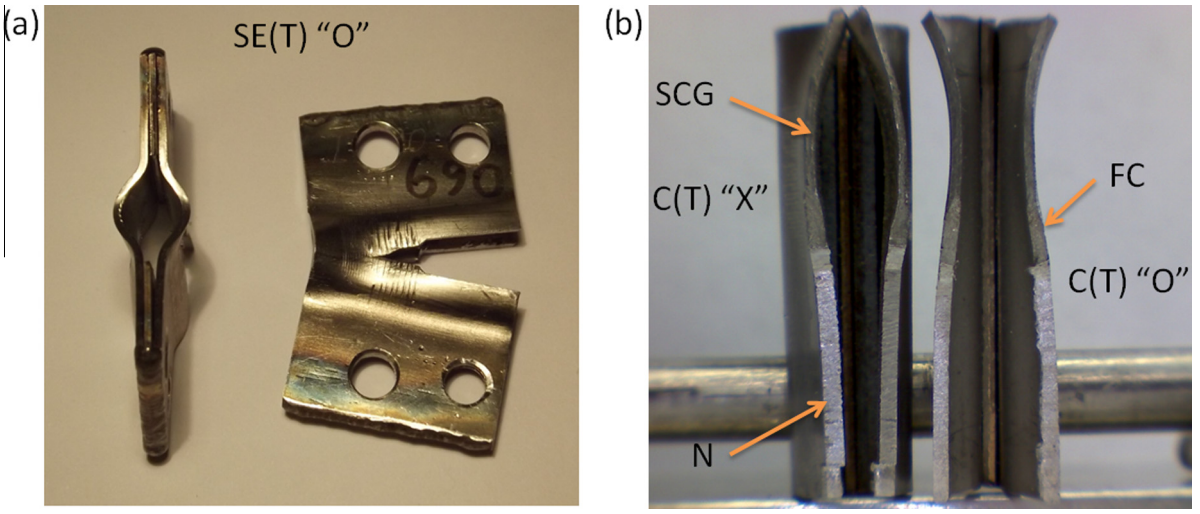

Fig. 15. Effects of plastic deformation and geometrical distortion in specimens with longitudinal TWCs (N: electric discharge machining induced notch, FC: fatigue crack, SCG: stable crack growth).

the fracture surfaces of C(T) "X" and C(T) "O" specimens. The curvature adopted by the initially straight remaining ligaments is evidenced. In the case of the C(T) "X" specimen, a separation between the initially in contact hemi-specimens was introduced. Similar behaviors to those presented in Fig. 15 were observed in the others specimens with longitudinal TWCs.

The above figures display the plastic deformation and geometrical distortion processes suffered by all the tested specimens during fracture tests. These experimental results supported the use of geometric nonlinearity or large deformation finite element analyses for the obtainment of the η-factors calculated in previous works [13,14]. In that way, due consideration was made of the changes in the loading conditions generated in the cracked section as a result of the specimens' deformation, of the development of bending components and of the realignment of remaining ligament with the loading axis due to the large displacements associated with the geometrical distortion.

Paris et al. [30] noticed that the development of an extended plastic deformation in fracture specimens tends to invalidate the η-factor existence. As showed by Bergant et al. [13,14], this effect is revealed as a η-factor dependence with the loading level. It was found, for instance, that the η-factors for T1(T) specimens have a higher dependence with the loading level than that for T1(B) specimens. These numerical results can be understood in terms of the different deformation behaviors observed for these specimens as was illustrated in Fig. 14(a) above.

5. Conclusions

The present work focused on practical aspects of the J-resistance curve evaluation of steam generator tubes used in the nuclear industry. The main conclusions that could be drawn from the study which are considered relevant for an adequate experimental characterization are summarized in what follows.

During pre-cracking stage it was found that longitudinal TWCs developed inclined fronts, i.e., not normal to the tube surfaces, due to the effect of an extra bending component generated by the tube curvature. This effect was higher for M(T) "O" specimens leading to uneven growth of the crack fronts. For that reason, it was disregarded for fracture testing.

The crack growth measurements throughout fracture tests were performed by an optical technique at the specimen's surface. Tunneling tests demonstrated that the error in the estimation of the crack extension from the direct optical surface measurement is reduced. Therefore, the optical technique was considered adequate for the aim of this work. Alternatively, the NDRM was applied to several tests, giving quite acceptable results compared with the optical measurements. This method can be applied in high temperature tests corresponding to SGTs operating conditions.

J-resistance curves for each testing configuration gave almost identical results for both η_{LLD} and η_{CMOD} definitions as long as the specimen had deep cracks ($a/W \sim 0.5$), demonstrating that are equally valid for an appropriate evaluation of J-integral values.

J-resistance curves obtained in this work evidenced anisotropy and constraint effects: circumferential TWCs led to higher curves than longitudinal TWCs, while tensile loadings with lower constraint gave slightly raised curves than bending configurations with higher constraint conditions.

It was shown that all the proposed specimens (exempting the M(T) "O") in combination with the optical or the NDRM techniques permit a suitable experimental determination of fracture properties that can be used in structural integrity assessments of cracked SGTs.

Finally, it is worth emphasizing that the η-factors and J-resistance curves presented are strictly valid to the specimens and tube geometries used in this work. The fracture toughness reported should be considered as specific to the SGT geometry studied and are not a material property.

Acknowledgments

This work was supported by the Argentine National Atomic Energy Commission (Comisión Nacional de Energía Atómica, CNEA). The authors thank FAE SA for the provision of SGTs used in this research.

References

[1] EPRI. Steam generator integrity assessment guidelines. Revision 2, Technical Report 1012987; 2006.
[2] IAEA-TECDOC-1668: assessment and management of ageing of major nuclear power plant components important to safety: steam generators. International Atomic Energy Agency; 2011 update.
[3] Cizelj L, Mavko B, Riesch-Oppermann H, Brucker-Froit A. Propagation of stress corrosion cracks in steam generator tubes. Int J Press Ves Pip 1995;63:35–43. http://dx.doi.org/10.1016/0308-0161(94)00046-L.
[4] Majumdar S. Failure and leakage through circumferential cracks in steam generator tubing during accident conditions. Int J Press Ves Pip 1999;76:839–47. http://dx.doi.org/10.1016/S0308-0161(99)00058-7.
[5] Lee J, Park Y, Song M, Kim Y, Moon S. Determination of equivalent single crack based on coalescence criterion of collinear axial cracks. Nucl Eng Des 2001;205:1–11. http://dx.doi.org/10.1016/S0029-5493(00)00368-X.
[6] Park Y, Song M, Lee J, Moon S, Kim Y. Investigation on the interaction effect of two parallel axial through-wall cracks existing in steam generator tube. Nucl Eng Des 2002;214:13–23. http://dx.doi.org/10.1016/S0029-5493(02)00010-9.
[7] Wang X, Reinhardt W. On the assessment of through-wall circumferential cracks in steam generator tubes with tube supports. J Press Ves Technol 2003;125:85–90. http://dx.doi.org/10.1115/1.1511737.
[8] Tonkovic Z, Skozrit I, Soric J. A contribution to assessment of steam generator tubes integrity. In: 11th international conference on fracture, 01/2005, 4. Turin, Italy; 2005.
[9] Chang Y, Kim Y, Hwang S, Kim J. Burst pressure estimation of steam generator tubes based on fracture mechanics analyses. Key Eng Mater 2006;321–323:666–9. http://dx.doi.org/10.4028/www.scientific.net/KEM.321-323.666.
[10] Huh N, Kim J, Chang Y, Kim Y, Hwang S, Kim J. Elastic-plastic fracture mechanics assessment for steam generator tubes with through-wall cracks. Fatigue Fract Eng Mater Struct 2006;30:131–42. http://dx.doi.org/10.1111/j.1460-2695.2006.01094.x.
[11] Tonkovic Z, Skozrit I, Alfirevic I. Influence of flow stress choice on the plastic collapse estimation of axially cracked steam generator tubes. Nucl Eng Des 2008;238:1762–70. http://dx.doi.org/10.1016/j.nucengdes.2008.01.008.
[12] Hu J, Liu F, Cheng G, Zhang Z. Determination of the critical crack length for steam generator tubing based on fracture-mechanics-based method. Ann Nucl Energy 2011;38:1900–5. http://dx.doi.org/10.1016/j.anucene.2011.05.009.
[13] Bergant M, Yawny A, Perez Ipiña J. Estimation procedure of J-resistance curves for through wall cracked steam generator tubes. Proc Mater Sci 2012;1:273–80. http://dx.doi.org/10.1016/j.mspro.2012.06.037.
[14] Bergant M, Yawny A, Perez Ipiña J. Numerical study of the applicability of the η-factor method to J-resistance curve determination of steam generator tubes using non-standard specimens. Eng Fract Mech 2015;146:109–20. http://dx.doi.org/10.1016/j.engfracmech.2015.07.059.
[15] Bergant M, Yawny A, Perez Ipiña J. Failure assessment diagram in structural integrity analysis of steam generator tubes. Proc Mater Sci 2015;8:128–38. http://dx.doi.org/10.1016/j.mspro.2015.04.056.
[16] Bergant M, Yawny A, Perez Ipiña J. Structural integrity assessments of steam generator tubes using the FAD methodology. Nucl Eng Des 2015;295:457–67. http://dx.doi.org/10.1016/j.nucengdes.2015.09.022.
[17] Sanyal G, Samal M. Assessment of axial cracking of a steam generator tube. J Metall Eng 2012;1:53–62.
[18] Sanyal G, Samal M. Investigation of fracture behavior of steam generator tubes of Indian PHWR using PLT specimens. Proc Eng 2013;55:578–84. http://dx.doi.org/10.1016/j.proeng.2013.03.298.
[19] Rice J, Paris P, Merkle J. Some further results of J-integral analysis and estimates. In: Progress in flaw growth and fracture toughness testing, ASTM STP 536. p. 231–45. http://dx.doi.org/10.1520/STP49643S.
[20] ASTM A370-15 standard test methods and definitions for mechanical testing of steel products. American Society for Testing and Materials; 2015. http://dx.doi.org/10.1520/A0370-15.
[21] Sumpter J, Turner C. Method for laboratory determination on J_c. In: Cracks and Fracture, ASTM STP 601. p. 3–18. http://dx.doi.org/10.1520/STP28634S.
[22] Ernst H, Paris P, Landes J. Estimations on J-integral and tearing modulus T from a single specimen test record. In: Roberts R, editor. Fracture mechanics: thirteenth conference, ASTM STP 743. American Society for Testing and Materials; 1981. p. 476–502. http://dx.doi.org/10.1520/STP28814S.
[23] Dawicke DS, Sutton MA. Crack-tip-opening angle measurements and crack tunneling under stable tearing in thin sheet 2024-T3 aluminum alloy. Nasa Contract Report 191523. Langley Research Center; 1993.
[24] James MA, Newman JC. Characterization of crack length measurement methods for flat fracture with tunneling. J ASTM Int 2005;2(3):506–20. http://dx.doi.org/10.1520/JAI12053.
[25] ASTM E1820-15 standard test method for measurement of fracture toughness. American Society for Testing and Materials; 2015. http://dx.doi.org/10.1520/E1820-15.
[26] Wallin K. Fracture toughness of engineering materials, estimation and application. Warrington, UK: EMAS Publishing; 2011.
[27] Wilkowski GM, Maxey WA. Review and applications of the electric potential method for measuring crack growth in specimens, flawed pipes, and pressure vessels. In: Fracture mechanics: fourteenth symposium – volume II: testing and applications, ASTM STP 791. p. 266–94.
[28] Cerný I. The use of DCPD method for measurement of growth of cracks in large components at normal and elevated temperatures. Eng Fract Mech 2004;71:837–48. http://dx.doi.org/10.1016/S0013-7944(03)00012-2.
[29] Landes JD. The blunting line in elastic-plastic fracture. Fatigue Fract Eng Mater Struct 1995;18:1289–97. http://dx.doi.org/10.1111/j.1460-2695.1995.tb00855.x.
[30] Paris P, Ernst H, Turner C. A J-integral approach to development of η-factors. In: Fracture mechanics: twelfth conference, ASTM STP 700. p. 338–50. http://dx.doi.org/10.1520/STP36979S.